ORIGINAL PAPER

Interfacial structure changes between amorphous silicon anode/liquid electrolyte using a highly dense and flat model electrode

Sho Asano[1] · Jun-ichi Hata[1] · Kenta Watanabe[1] · Naoki Matsui[2] · Kota Suzuki[2] · Ryoji Kanno[2] · Masaaki Hirayama[1,2]

Abstract

Changes in the interfacial structures of the amorphous silicon (a-Si) anode/organic electrolyte interfaces in lithium-ion batteries were investigated using highly dense a-Si films fabricated by cathodic arc plasma deposition as a model electrode. Raman spectroscopy, transmission electron microscopy (TEM), and X-ray reflectivity revealed that the Si films were grown in an amorphous state with an atomically flat surface. The a-Si films exhibited lithium alloying and de-alloying reactions, with a large irreversible capacity during the first cycle. The irreversible capacity was derived from the formation of a solid electrolyte interphase (SEI) along with an incompletely de-alloyed Li-Si phase, as confirmed by ex situ TEM and X-ray photoelectron spectroscopy observations. The discharge and charge capacities of the Si films gradually decreased in the subsequent cycles, despite the fact that no further SEI formation or cracking of the Si layer occurred. Scanning electron microscopy observations combined with energy-dispersive X-ray spectroscopy revealed the miniaturization of the a-Si film in the surface region to generate domains measuring less than a few hundred nanometers. These results suggest that delamination and miniaturization of the a-Si nanodomains from the electrode surface are partly responsible for degradation of the a-Si anode.

Keywords Silicon anode · Model electrode · Cycle stability · Interfacial structure · Arc plasma deposition

Introduction

Lithium-ion batteries (LIBs) are commonly used as representative rechargeable batteries for electric devices, including laptop computers and smartphones. In recent years, LIBs have also been employed in large applications, such as electric vehicles and megawatt power sources for renewable energy. However, to render such applications more viable, it is necessary to improve the energy densities of LIBs. As a prospective anode candidate for LIBs, silicon has been considered due to its high energy density. Silicon anodes are known to form a $Li_{4.4}Si$ alloy via an electrochemical reaction with lithium under low voltage conditions (< 0.3 V vs. Li/Li$^+$), leading to a high energy density of 788 Wh kg^{-1} when combined with a LiCoO$_2$ cathode [1]. This energy density is significantly higher than those of other conventional anode materials such as graphite (ca. 584 Wh kg^{-1}) and Li$_4$Ti$_5$O$_{12}$ (ca. 178 Wh kg^{-1}) [2–4]. Furthermore, silicon is a desirable material due to its abundance in nature and its high Clarke number [4].

However, despite such advantages, Si anodes suffer from a severe decrease in capacity during charge–discharge cycling, which originates from an extreme volumetric expansion of 300–400% during lithium alloying [5–7]. This volumetric change causes particle fractures and crack generation, resulting in disconnections in the electronic and ionic conduction pathways [8]. In the case of crystalline silicon (c-Si), an anisotropic expansion along the crystalline orientation takes please easily under concentrated stress conditions to cause particle fractures [6, 9]. However, such fractures can be suppressed in amorphous silicon (a-Si) because of its isotropic expansion, which ultimately leads to improved cycle stabilities [9, 10]. As such, previous works have attempted to control the morphology of a-Si through nanosizing, compositing, and porosifying to further suppress fracture formation [9, 11–13]. The cycle degradation of Si anodes is also partly attributed to the side reactions that take place at the

✉ Masaaki Hirayama
hirayama@mac.titech.ac.jp

[1] Department of Chemical Science and Engineering, School of Materials and Chemical Technology, Tokyo Institute of Technology, 4259 Nagatsuta, Midori–ku, Yokohama 226–8502, Japan

[2] Research Center for All–Solid–State Battery, Institute of Innovation Research, Tokyo Institute of Technology, 4259 Nagatsuta, Midori–ku, Yokohama 226–8502, Japan

electrode/liquid electrolyte interface. More specifically, a solid electrolyte interphase (SEI) is formed at the electrode surface upon reaction with lithium ions and decomposed electrolyte species [14]. Although the SEI can enhance the cycle stability by the suppression of further side reactions [15], a large SEI is known to interfere with the electronic and ionic conduction properties [13]. In such cases, electrolyte decomposition proceeds at the newly generated Si surfaces to reduce the interfacial ionic conductivity during cycling [16, 17]. However, it is difficult to analyze the electrochemical processes taking place at Si/electrolyte interfaces separately from mechanical factors owing to their complicated electrode structures.

To address such issues, thin-film electrodes with flat and uniform surfaces have been considered due to the fact that they provide a simple reaction field for investigating the nanoscale interfacial phenomena [18, 19]. For example, analysis of the reaction taking place at the c-Si film/liquid model interface was conducted using extremely flat c-Si films with a surface roughness of 1–2 nm. These investigations revealed the growth process of the SEI, along with different alloying degrees between the surface region and the bulk [20]. In contrast, the majority of a-Si films fabricated by conventional chemical vapor deposition and sputtering approaches exhibit surface roughnesses in the range of 15–50 nm [21, 22], likely due to the low synthetic temperatures employed (approximately 100 °C), which are insufficient to yield a flat surface [22]. As a result, few mechanistic studies have been conducted on the interfacial reactions between Si and liquid electrolytes using a-Si films with flat surfaces [23].

In this study, a-Si film electrodes are fabricated via cathode arc plasma deposition (CAPD), which is a technique that is commonly used to fabricate atomically flat amorphous films [24, 25]. The crystallinity and morphology of the fabricated silicon films are then evaluated using Raman spectroscopy, transmission electron microscopy (TEM), and X-ray reflectivity (XRR) to verify the dense and flat natures of the films. Subsequently, the discharge–charge properties at the interface between the a-Si and an organic liquid electrolyte are examined using constant current charge–discharge tests with coin-type cells using a lithium metal counter electrode. Moreover, the chemical and morphological changes at the interfaces are investigated after the initial charge–discharge cycles using X-ray photoelectron spectroscopy (XPS), scanning electron microscopy (SEM), and energy-dispersive X-ray spectroscopy (EDX). Finally, the changes in the interfacial structure between the a-Si and the liquid electrolyte are investigated, and the effects of the interfacial structure on the battery performance are discussed based on SEI formation and the miniaturization of a-Si at the electrode surface.

Methods

Synthesis of the silicon films

The silicon films were fabricated using the CAPD (ADVANCE RIKO, APD-1S, see Fig. S1) method. A B-doped silicon target (resistance 0.01 Ω cm, TOSHIMA Manufacturing, Saitama, Japan) coated with carbon on the target surfaces was employed. Carbon coating and B-doping were conducted to maintain a suitable electrical conductivity and to stabilize the plasma discharges. Single-crystal Al_2O_3 substrates (10×10 mm^2, Crystal Base, Osaka, Japan), Cu substrates (10×10 mm^2, Crystal Base, Osaka, Japan), and foils (φ10 mm) were employed. The fabrication conditions were as follows: discharge voltage = 200 V, capacitance = 360 μF, frequency of discharge = 3 Hz, distance from the target to the substrate = 80 mm, and pressure approximately 5.0×10^{-5} Pa. The substrates were rotated at 15 rpm during CAPD to ensure uniform fabrication.

Structural characterization

The crystallinity of each films was characterized by Raman spectrometry (XploRA PLUS, Horiba, Kyoto, Japan) with a 532-nm excitation laser (10 mW) using an airtight cell. High-resolution (HR) TEM observations (JEM-2100, JEOL, Tokyo, Japan) were performed to evaluate the crystallinity and density of each Si films. Using direct current (DC) sputtering, the Si surfaces were covered with a 150-nm-thick Au film as a conductive layer, and subsequently focused ion beam (FIB) deposition was used to introduce a 500-nm-thick carbon film and to prepare in the shape of flakes [26]. The TEM samples were then transferred to a vacuum chamber under air exposure. HR-TEM images were collected at an accelerating voltage of 200 kV. The thickness, scattering length density (SLD), and roughness of the Si films were determined by XRR. The XRR measurements were performed under an air environment using an X-ray diffractometer with Cu Kα radiation (ATX-G, Rigaku, Tokyo, Japan).

Electrochemical characterization

2032-Type coin cells were assembled in an argon-filled glovebox using a-Si/Cu as the working electrode (cathode), Li foil (99.8%, Honjo Metal, Osaka, Japan) as the counter electrode (anode), and a 1 mol dm^{-3} solution of $LiPF_6$ containing ethylene carbonate and diethyl carbonate (3:7 by volume) as the liquid electrolyte. Galvanostatic charge–discharge tests were conducted in the 0.02–1.5 V range at room temperature using a potentiostat/galvanostat (TOSCAT, Toyo system, Fukushima, Japan). The

Fig. 1 **a** Surface Raman spectrum, **b** cross-sectional HR-TEM (500 K) image, and **c** observed and calculated XRR spectra of the Si films synthesized by CAPD at room temperature. **d** SLD profile calculated using the structural parameters refined by XRR analysis. The XRR fitting model is shown in the inset of part (c)
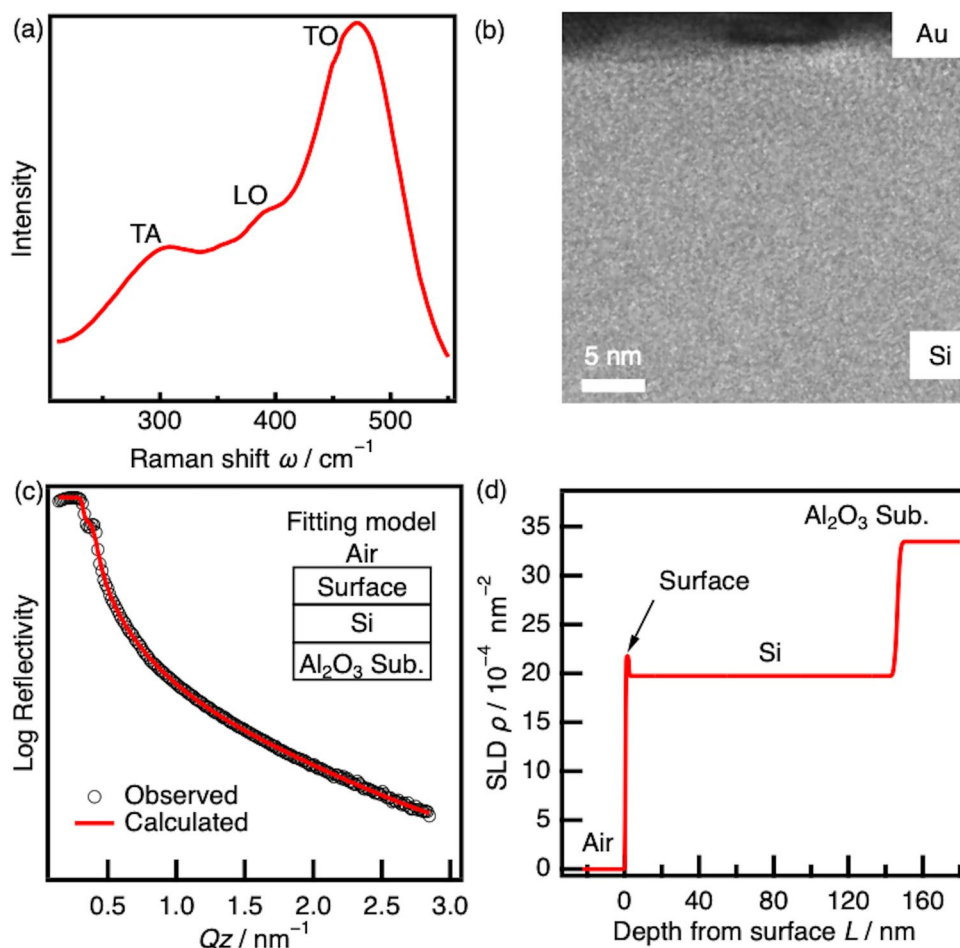
current density was set to 4200 mA g^{-1}. The weight of the Si film anode was calculated using the deposition area (0.78 cm^2, diameter φ10 mm), the theoretical density of Si (2.33 g cm^{-3}), and the thickness determined obtained via XRR (150 nm). The specific capacities were calculated using the weight of Si and the amount of electricity obtained from the galvanostatic charge–discharge tests.

Ex situ HR-TEM, XPS, and SEM analyses

After the discharge–charge cycles, the coin cells were disassembled in an Ar-filled glovebox. The Si/Cu samples were washed with dimethyl carbonate and dried using a blower. The morphological changes in the Si film were investigated using high-resolution transmission electron microscopy (HR-TEM; JEM-2100, JEOL). The sample transfer and measurement conditions were the same as those used for the pristine Si film described above. The chemical and morphological changes taking place in the interfacial structures were evaluated by XPS (ULVAC-PHI, ESCA 1700R, Kanagawa, Japan) using focused monochromatized Al Kα radiation ($h\nu = 1486.6$ eV) in combination with field-emission (FE), and SEM (Hitachi High-Tech; Regulus 8230, Tokyo, Japan) and EDX (Bruker,

QUANTAX FlatQUAD, MA, USA). The Si/Cu samples were transferred to XPS and SEM/EDX chambers using airtight transfer vessels to minimize chemical and the morphological changes at the sample surface during the analytical process. During the XPS measurements, the Si 2p, C1s, O 1 s, F 1 s, and Cu 2p spectra were collected for each sample after discharge–charge cycling. All spectra were recorded at a pass energy of 23.5 eV. Charge neutralization was not employed. CasaXPS software [27] was used to fit the XP spectra, and the binding energy scale was calibrated based on the hydrocarbon C 1 s peak at 284.8 eV [28]. The FE-SEM and EDX images were collected at an acceleration voltage of 15 keV and an emission current of 14.8 µA.

Results and discussion

Structures of the CAPD-fabricated Si films

Figure 1a shows the Raman spectrum of the Si film fabricated using CAPD at room temperature. This spectrum exhibited a broad peak at approximately 470.7 cm^{-1}, which corresponds to the transverse optical (TO) phonons

Table 1 Refined thickness, SLD, and roughness value for each Si film deposited by CAPD ($\chi^2 = 6.20 \times 10^{-4}$). χ^2 represents the accuracy of the fitting. The XRR spectrum and fitting model are shown in Fig. 1c

Component	Thickness, d (nm)	SLD (10^{-4} nm^{-2})	Roughness, σ (nm)
Surface layer	1.9	21.8	0.2
Si	144.0	19.7	0.2
Al$_2$O$_3$	–	33.5 (fixed)	1.2

present in a-Si [29]. The weak shoulders observed at 400 and 300 cm^{-1} were derived from longitudinal optical (LO) phonons and transverse acoustic (TA) phonons, respectively. However, no sharp peak derived from the TO phonons of c-Si was observed at 520 cm^{-1} [29]. In addition, as shown the HR-TEM image (Fig. 1b), no lattice fringes were observed in the Si film. Thus, in combination, these results indicate the formation of an a-Si film. Figure 1c presents the XRR fitting results for a Si film grown on Al$_2$O$_3$(0001), wherein the observed spectrum fits closely with a two-layer model comprising the surface and Si layers. The refined thickness, scattering length density (SLD), and roughness of each layer are summarized in Table 1. From these values, it can be seen that the Si film layer exhibited an SLD value of 19.7×10^{-4} nm^{-2}, which is slightly lower than the theoretical SLD of c-Si (i.e., 20.1×10^{-4} nm^{-2}) [30–32], thereby confirming the formation of dense a-Si layer on the substrate. Furthermore, the thickness and SLD of the surface layer were determined to be 1.9 nm and 21.8×10^{-4} nm^{-2}, respectively. Since the XRR measurements were conducted

under an air atmosphere, reaction between the Si surface and oxygen present in the air could generate a surface layer consisting of Si oxides, such as SiO$_2$ (22.7×10^{-4} nm^{-2}) [30–32] and SiO$_x$ ($x = 1.0$: 18.3×10^{-4} nm^{-2}, $x = 1.6$: 19.3×10^{-4} nm^{-2}) [31, 33]. Furthermore, it was deduced that the surface and interfacial roughness were < 1.2 nm. These structural parameters therefore confirm the successful CAPD-based room-temperature synthesis of highly dense a-Si films with an atomically flat surface, which provides a homogeneous Si anode–liquid electrolyte interface with a defined area. These systems can therefore be considered suitable for use in investigating the interfacial phenomena.

Electrochemical activities of the CAPD-fabricated a-Si films

Figure 2 shows the discharge–charge curves, dQ/dV plots, capacity retention capability, and Coulombic efficiency of a 150-nm-thick a-Si film deposited on Cu, wherein these plots were obtained during the initial five cycles. The first discharge curve shows two sloped regions at approximately 0.20 and 0.09 V, which correspond to formation of Li–Si alloys according to the following two steps: Si → Li$_x$Si and Li$_x$Si → Li$_y$Si ($x < y$), respectively [34, 35]. In addition, the sloped regions observed at 0.30 and 0.45 V during the first charge indicate de-lithiation of the Li–Si alloy. The first discharge and charge capacities were determined to be 3825 and 3298 mAh g^{-1}, respectively, with an irreversible capacity of 528 mAh g^{-1} (3.40 μAh cm^{-2}). In the dQ/dV plots, weak reduction peaks were observed at approximately 1.2 and 0.8 V during the first discharge, and

Fig. 2 **a** Discharge–charge curves, **b** dQ/dV plots, **c** capacity retention plot, and **d** Coulombic efficiency plot for a 150-nm-thick a-Si anode. The current density was set to 4200 mA g^{-1}
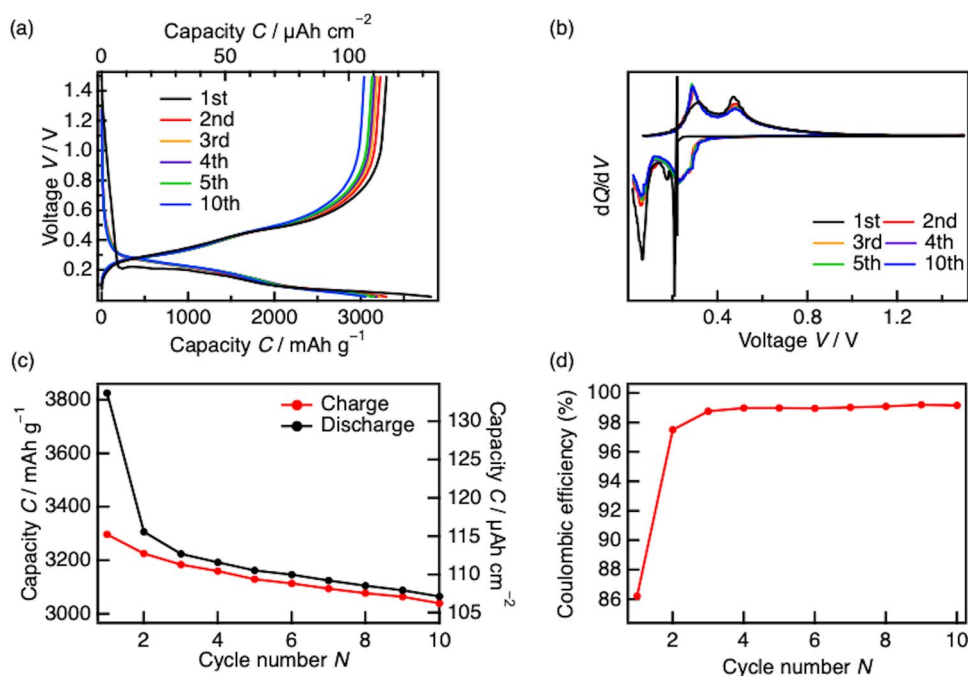
which were attributed to decomposition of the electrolyte species [14]. Notably, no reduction peaks were observed in these voltage regions in the subsequent cycles. Furthermore, the reduction peak observed at 0.09 V during the first discharge was more intense than the corresponding peak during the subsequent cycles, indicating that the electrolyte decomposition proceeded further at low voltages. These results therefore reveal that electrolyte decomposition during the initial discharge process contributed to the irreversible capacity observed for this system.

Beyond the second cycle, the shapes of the discharge and charge curves remained relatively constant, demonstrating that reversible lithiation and delithiation took place in the a-Si film anode. In addition, it was found that the irreversible capacity significantly decreased to 82.4 mAh g^{-1} in the second cycle. Based on this result, it was hypothesized that the decomposition product generated during the initial discharge may act as an SEI, which suppresses further decomposition of the electrolyte species. The rapid decrease in the irreversible capacity also indicates that a dense and rigid SEI layer was formed on the flat Si surface during the initial discharge. As a result, the Coulombic efficiency increased from 86.2% in the first cycle to 97.5% in the second cycle, and this value further increased with subsequent cycles to reach 99.0% in the fifth cycle. Although the side reactions between the Si film and the liquid electrolyte were suppressed by the SEI layer, the discharge–charge capacities decreased gradually during the initial five cycles. Whereas the discharge–charge capacities continued to decrease gradually in the subsequent cycles (see Fig. S2), the capacity retention plot showed an inflection point at approximately the twentieth cycle. This result implies that the a-Si anode deteriorates via different mechanisms depending on the cycle number. In this study, we focused on the early stage of the deterioration process at the Si/electrolyte interface, which has been less well-recognized previously.

Changes in the interfacial structure at the a-Si–electrolyte interface

To gain an improved understanding of the cycle degradation process taking place at the a-Si–electrolyte interface, ex situ TEM and XPS analyses were conducted after the discharge–charge reactions. Figure 3 shows the TEM images obtained for the pristine a-Si film and the film after the first cycle. In both cases, dense films with flat surfaces were observed, indicating that no cracks or cavities were formed in the film structure during the initial lithiation and delithiation processes. The a-Si-film anode therefore provides a model interface to eliminate changes in the reaction area induced by microstructural changes within the electrode. Notably, the cycled film showed a slight increase in thickness from 58.7 to 61.3 nm, indicating a volumetric expansion of 4%. As previously reported, the volume of an Si anode expands by approximately 300% during lithium alloying (discharging) and shrinks reversibly during de-alloying (charging) [10]. Considering that no cracks and voids were observed inside the electrode during the initial cycle, the increase in volume indicates that the Li–Si alloy was not fully delithiated during the initial charging process [36]. It is therefore possible that the Li$_x$Si alloy ($x=0$) present in the interfacial regions may be thermodynamically and/or kinetically stabilized. Assuming that the volume of a-Si has a linear relationship with the lithium content, the composition of Li–Si with a volumetric expansion of 4% was estimated to be Li$_{0.18}$Si, which corresponds to an irreversible capacity of 56 mAh g^{-1}. This value is significantly smaller than the irreversible capacity of 528 mAh g^{-1} observed in the first discharge–charge curves (Fig. 2). These results reveal that the first irreversible capacity was predominantly derived from side reactions at the a-Si–electrolyte interface, such as electrolyte decomposition and SEI formation. However, the SEI layer was not observed in the HR-TEM image obtained for the a-Si surface after the initial cycle, thereby suggesting that the SEI layer may be removed during the washing process and/or damaged during FIB-based sample fabrication.

Fig. 3 HR-TEM ($\times$100,000 resolution) images of the Si anode **a** before (pristine) and **b** after the first cycle
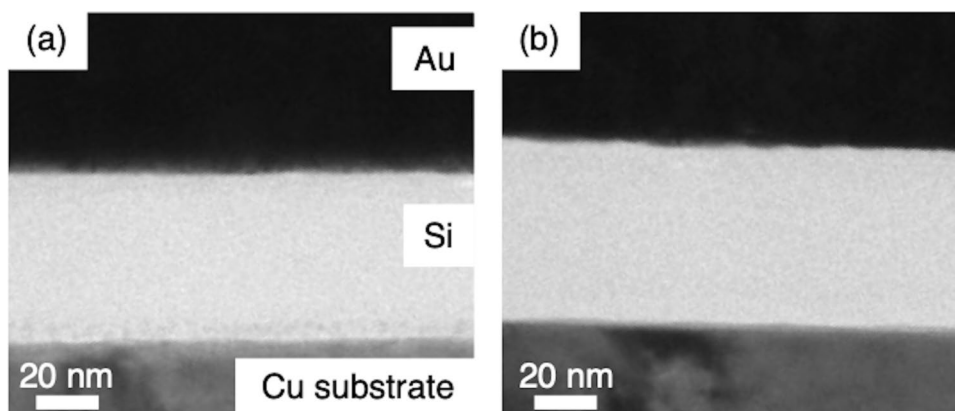
Ex situ XPS analyses were subsequently performed to clarify the side reactions taking place at the a-Si–electrolyte interface. Figure 4 shows the Si 2p XP spectra of the Si films in the pristine state and after the first, second, third, fourth, and fifth charging (de-alloying) steps, wherein a significant decrease in the Si signal intensity can be seen for the cycled films compared with that observed for the pristine film. Considering the short escape depth of the photoelectrons generated by Al Kα X-ray irradiation, it appeared that the Si film surfaces were covered by the SEI layer formed during the initial discharge–charge process, as also indicated by the discharge–charge and HR-TEM analyses. In addition, the decrease in the Si signal intensity became less pronounced after the second and subsequent charges, indicating that no further growth of the SEI layer took place after the first discharge. This agrees with the significant decrease detected for the irreversible capacity after the second cycle (Fig. 2). Furthermore, in the pristine conditions, the Si 2p peaks were observed at 99.8 and 99.2 eV, correlating to Si–Si bonding in the Si film [37]. These peak positions shifted slightly to 99.5 and 98.9 eV after the first de-alloying step. Indeed, it has been previously reported that the Si–Si peaks shift to
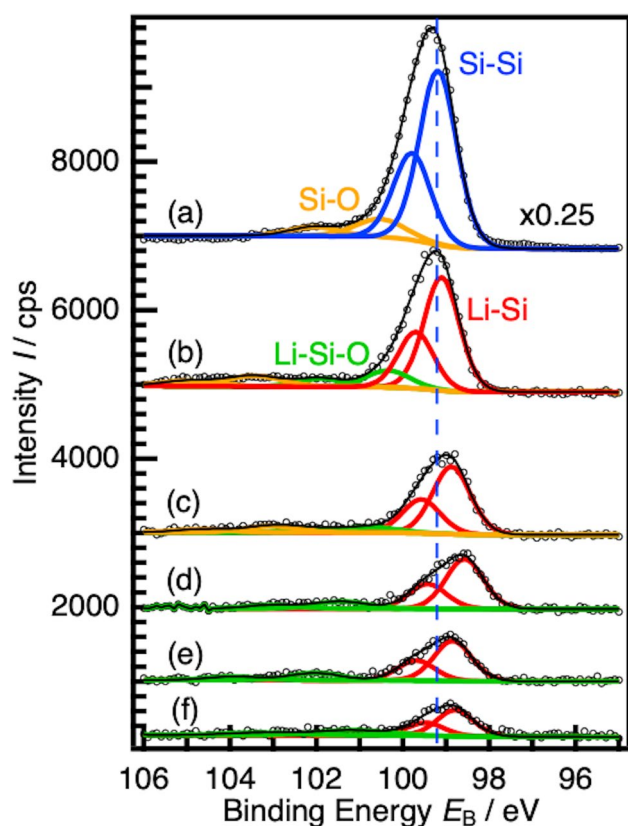
lower binding energies (98.0–96.0 eV) upon lithium alloying [37]. Therefore, it is suggested that the a-Si film electrode occurred the incomplete delithiation of the Li–Si alloy, as also suggested by ex situ TEM imaging (Fig. 3). In the subsequent cycles, the Si 2p peaks were observed at lower binding energies than those in the pristine a-Si film, suggesting that the alloying and de-alloying reactions proceeded reversibly in a limited composition region after the first cycle.

To investigate the chemical species present in the SEI layer, the C 1 s, O 1 s, and F 1 s XP spectra were analyzed by multi-peak fitting, and Fig. 5 shows the fitting results of the C 1 s, O 1 s, and F 1 s spectra for the pristine and cycled a-Si film anodes. In addition, Fig. 6 summarizes the atomic ratios of the chemical components determined from the Si 2p, C 1 s, O 1 s, and F 1 s spectra. For the pristine a-Si film, C 1 s and O 1 s peaks were observed at 282.7 and 532.0 eV (Figs. 5a and 6(b)), corresponding to the Si–C [38] and Si–O [39] bonds, respectively. These components are impurities introduced into the film during the CAPD process, and they originate from the carbon-coated Si target and the presence of residual oxygen in the CAPD chamber. After the first charge, peaks corresponding to C–O, O–C=O, CO_3, Li–Si–O, P–O–F, P–F, and Li–F bonds were observed in the C 1 s, O 1 s, and F 1 s spectra, indicating the presence of electrolyte decomposition products, such as Li_2CO_3, Li-Si–O, LiF, Li-P-O-F, and lithium alkyl carbonate [40–42]. These compounds were formed on the Si surface during generation of the SEI layer. After the second charge process, no significant changes were observed in the XP spectra, and the atomic ratios of the SEI components remained relatively constant. However, the total atomic ratios of the SEI to Si components increased slightly, as can be seen in Fig. 6(b) and (c). The electronically insulating SEI layer therefore appeared to sufficiently suppress further decomposition of the electrolyte by disturbing its direct contact with the Si surface, leading to an increase in the Coulombic efficiency in the second cycle (Fig. 2). From the third to the fifth cycle, the atomic ratios of the SEI to the Si components showed little to no changes (Fig. 6(d–f)). During this period, growth of the SEI layer ceased, thereby corresponding with the sustained high Coulombic efficiencies of >98% during these cycles (Fig. 2d). However, it should be noted that a new Li–O component appeared in the O 1 s spectra at 528.8 eV, while the intensities of the P–F and P–O–F components gradually decreased in the F 1 s spectra (Fig. 5b and c). In terms of the atomic ratios, the ratio of the inorganic SEI species increased, while that of organic SEI species decreased (Fig. 6(d), (e), and (f)). As reported previously, the Li–O phase could not be formed by decomposition of the P–F and P–O–F components because these components decompose to generate LiF [23, 43]. In contrast, the organic SEI components can decompose to form Li_2CO_3, followed by further decomposition to generate Li_2O [41, 44–46]. These

Fig. 4 Si 2p XPS results for (a) the pristine a-Si film anode and the corresponding anode after the (b) first, (c) second, (d) third, (e) fourth, and (f) fifth charge (de-alloying) processes. Spectra of pristine a-Si thin film are shown in quarter intensity
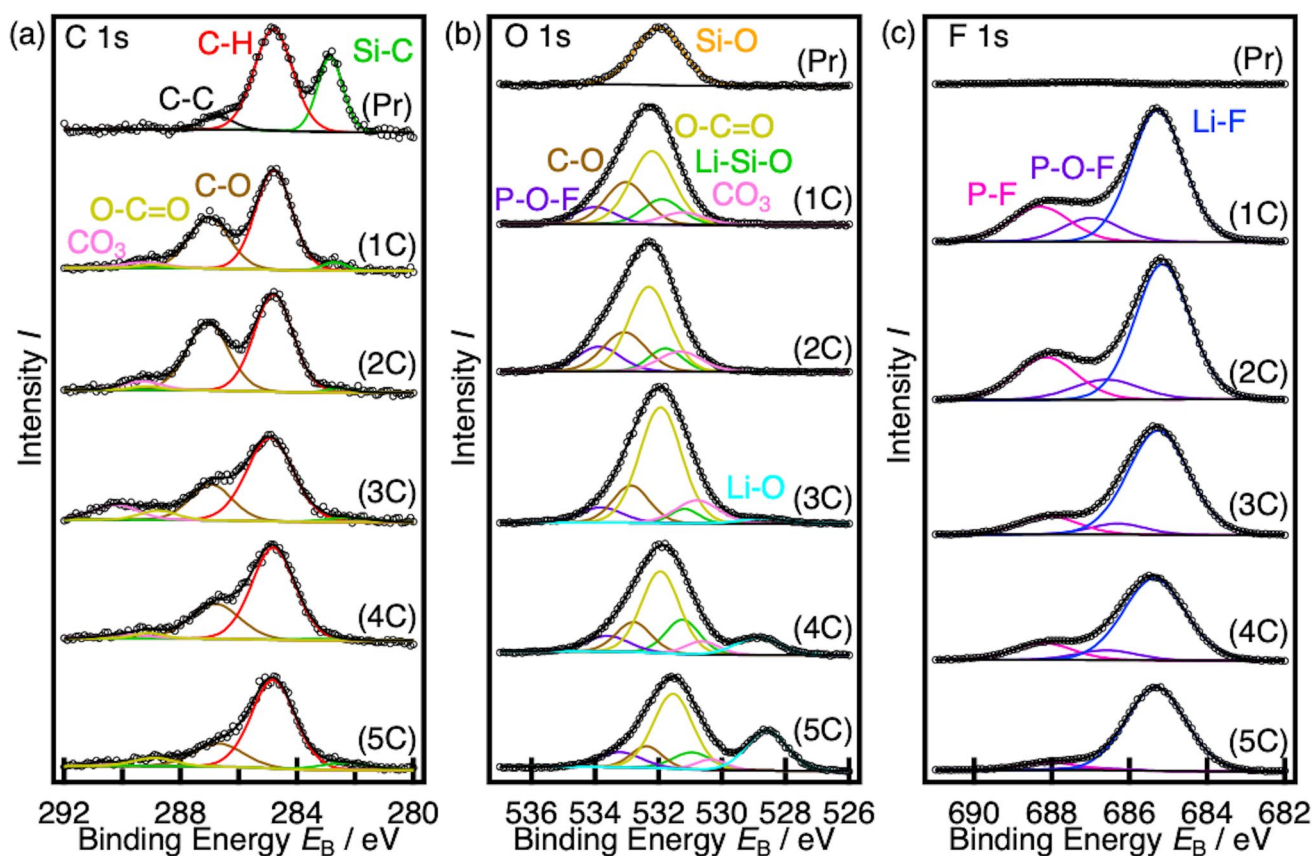
Fig. 5 **a** C 1 s, **b** O 1 s, and **c** F 1 s XP spectra of the (Pr) pristine a-Si film electrode and the corresponding electrodes after the (1C) first, (2C) second, (3C) third, (4C) fourth, and (5C) fifth charge (de-alloying) processes
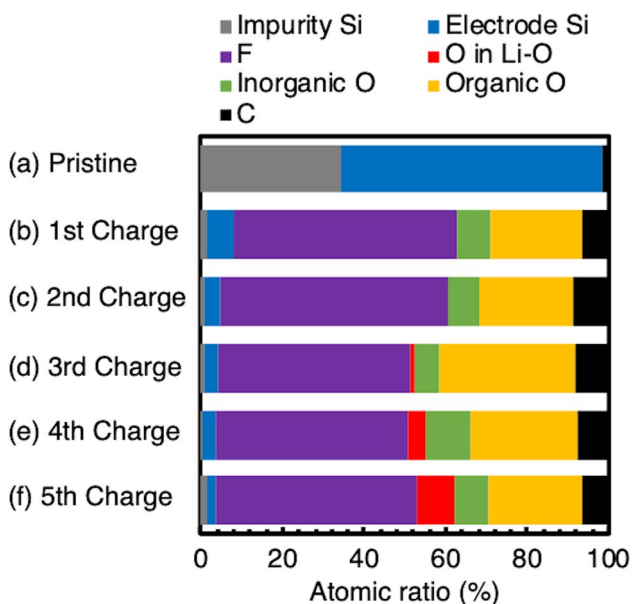

Fig. 6 Atomic ratios estimated from XP spectra and classified into C, organic O, inorganic O, O in Li–O, F, electrode Si, and impurity Si, for the a-Si film electrodes under different conditions: (a) the pristine electrode and the corresponding electrodes after the (b) first, (c) second, (d) third, (e) fourth, and (f) fifth charge processes

considerations suggest that decomposition of organic SEI species may result in a high ratio of inorganic SEI species during the initial cycles. Previously, density functional theory calculation results have indicated that Li$_2$O imparts rigidity to the SEI, which in turn promotes cracking of the Si layer [47]. Thus, compositional changes in the SEI layer during the first cycle may affect not only the electronic and ionic conductivities at the interface, but also the mechanical strength, thereby influencing the electrochemical stability at the a-Si–electrolyte interface in subsequent cycles.

Considering the results obtained by ex situ TEM and XPS analyses, it was clear that lithium alloying and de-alloying proceeded in the a-Si films with no severe microstructural changes and that any side reactions were sufficiently suppressed at the a-Si film surface after growth of the SEI layer (Figs. 3 and 6). Although these observations predict that the discharge–charge capacity should exhibit an excellent cycle stability, the discharge–charge measurements revealed a gradual decrease in the capacity, even in the initial five cycles (Fig. 2). These results therefore suggest that cross-sectional HR-TEM may not be suitable for observing the surface structural changes of the cycled a-Si films since it is difficult to distinguish them from the protective layer. Thus, surface SEM/EDX observations

were performed to investigate the structural changes taking place at the cycled Si surfaces to elucidate the physical factors responsible for the capacity decrease. Figure 7 shows the surface SEM/EDX images of the pristine Si film electrode along with those recorded for the same electrode after the first, third, and fifth cycles. More specifically, after the first cycle, a-Si domains of several hundred nanometers were formed. In addition, depressed regions were generated along the polishing lines of the Cu current collector, with very weak Si signals being observed between the a-Si domains. After the third cycle, elongated domains were clearly formed along the polishing lines of the Cu current collector, and depressed regions were clearly observed. It should be noted here that ex situ XPS did not detect any Cu 2p signals derived from the Cu current collector (see Fig. S3), thereby revealing that the Cu surface was not exposed to the electrolyte. It was therefore considered that the depressed regions may correlate with the difficulty of the characteristic X-rays escaping from inside the depression towards the detector in an oblique direction. These results indicate that the pristine a-Si film consisting of a smooth single domain was miniaturized by the mechanical stress resulting from volumetric changes during lithium alloying and de-alloying. After the fifth cycle, almost no structural changes were observed compared with the third cycle, while the capacities gradually decreased. It is therefore suggested that the a-Si nanodomains present at the surface are continuously delaminated by mechanical stress during the various cycles. Although it has been reported that the segregation of components originating from the decomposed electrolyte at the grain boundary can facilitate the pulverization of c-Si fragments [48], this has not been reported for a-Si electrodes. Indeed, the obtained XPS results revealed the formation and
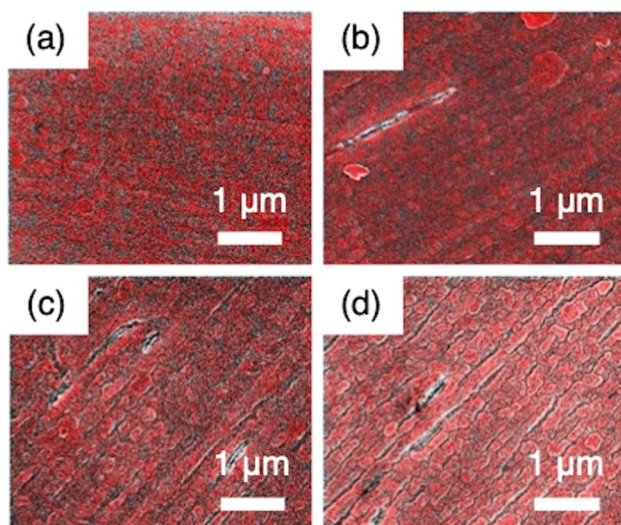
growth of Li_2O after the third cycle. The presence of this rigid Li_2O in the SEI [47] constrains the expansion and contraction of the a-Si electrode, suggesting that the miniaturization and delamination of the a-Si nanodomains occurred due to stress accumulation. With this in mind, the results obtained using the model electrode suggest that the a-Si nanodomain surface was miniaturized and delaminated during the initial cycles. Thus, even in the case of a-Si, whose mechanical properties are superior to those of c-Si, the mechanical factors originating from the mechanical stress caused by volume changes and SEI property changes are expected to affect the battery performance, including its surface miniaturization and delamination.

Initial phenomena at the Si anode–organic electrolyte interface

Based on the obtained discharge–charge, TEM, XPS, and SEM/EDX results, a schematic representation of the interfacial structures of the Si film during the initial alloying and de-alloying processes was constructed (Fig. 8). In the pristine condition, the Si film possessed an atomically flat surface with
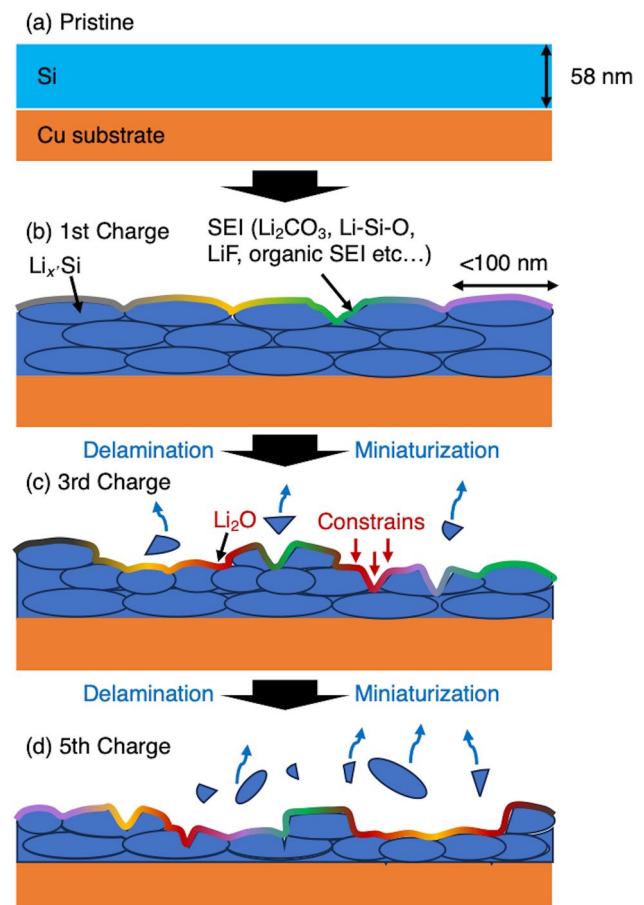
Fig. 7 SEM/EDX images of **a** the pristine Si anode and the same anode after the **b** first, **c** third, and **d** fifth charge

Fig. 8 Schematic images representing the interfacial structures in the (**a**) pristine state and after the (**b**) first, (**c**) third, and (**d**) fifth charges

a roughness of < 1.2 nm. In addition, it was observed that the Si consisted of a smooth single domain (Fig. 8(a)), containing high purity a-Si with some trace impurities (i.e., SiC, SiO$_2$, and SiO$_x$, x < 2). These results suggest that the fabricated a-Si film is suitable for use as a model electrode to investigate interfacial structures. In the initial cycle, discharge and charge capacities were 3825 and 3298 mAh g^{-1}, respectively, which gave an initial Coulombic efficiency of 86.2%. The TEM and XPS measurements revealed that lithium remained in the electrode after delithiation, and an SEI comprising Li$_2$CO$_3$, Li–Si–O, LiF, Li–P–O–F, and lithium alkyl carbonate was formed on the surface (Fig. 8(b)), leading to an irreversible capacity. Furthermore, a-Si nanodomains were observed on the electrode surface in addition to a depressed region that ran along the polishing lines of the Cu current collector. After the third cycle, the XPS peak intensity ratio between Si and the SEI species remained relatively constant, indicating that the formation of a dense SEI suppressed any further decomposition of the electrolyte species. Furthermore, TEM analysis revealed no significant changes in the film microstructures, which is consistent with the high Coulombic efficiency of > 98% achieved after the second cycle. However, the discharge and charge capacities gradually decreased during cycling, and the surface SEM images showed the presence of miniaturized a-Si nanodomains and some depressed regions on the electrode surface. These observations indicate that the gradual decrease in capacity may be caused by the delamination of a-Si nanodomains from the a-Si surface into the liquid electrolyte (Fig. 8(c)). After delamination, the a-Si surface became covered with newly formed SEI species due to electrolyte decomposition, thereby accounting for the absence of changes in the thickness of the SEI layer, as detected by XPS analyses (Fig. 8(c) and (d)). As indicated above, the delamination of miniaturized a-Si is mainly associated with the mechanical stress resulting from volumetric changes during (de)lithiation (Fig. 8(c) and (d)). In addition, the rigid Li$_2$O present in the SEI may lead to stress accumulation in the nanodomains (Fig. 8(c) and (d)). Indeed, it has been previously reported that the miniaturization and delamination of a-Si nanodomains are partly responsible for the degradation of c-Si electrodes [48]. Thus, in the current study, it was successfully demonstrated that the mechanical factors at the a-Si–liquid electrolyte interface have a significant effect on the cycle stability due to miniaturization and delamination of the a-Si nanodomains from the electrode surface.

Conclusion

A highly dense amorphous silicon (a-Si) film with an atomically flat surface was fabricated using cathode arc plasma deposition (CAPD), and its structure was confirmed by Raman spectroscopy, transmission electron microscopy, and X-ray reflectivity. The initial discharge capacity and coulombic efficiency were determined to be 3825 mAh g^{-1} and 86.2%, respectively (i.e., for the pristine electrode). Following the initial discharge–charge cycle, peaks originating from the solid electrolyte interphase (SEI) components (e.g., Li$_2$CO$_3$, Li–Si–O, LiF, Li–P–O–F, and lithium alkyl carbonate) were observed by ex situ X-ray photoelectron spectroscopy, indicating that SEI formation took place during the first cycle. This result therefore suggests that these chemical structural changes contributed to the irreversible capacity observed during the first cycle. In subsequent cycles, the capacity decreased gradually, whereas the Coulombic efficiency increased beyond 98%. This was attributed to the relatively consistent composition of the SEI components during cycling, in addition to the formation of Li$_2$O owing to the chemical decomposition reaction of the organic SEI species. Furthermore, ex situ scanning electron microscopy combined with energy dispersive X-ray spectroscopy indicated that the elongated surface a-Si domains became elliptical in nature, with widths of several hundred nanometers. Since no microstructural changes were observed in the films, the delamination and miniaturization of the a-Si nanodomains from the electrode surface caused by mechanical stress originated from volume changes and the changes in the mechanical properties of the SEI attributed to the presence of rigid Li$_2$O appeared to account for the gradual capacity decrease over subsequent cycles. Consequently, using the a-Si model electrode fabricated by CAPD, it was revealed that the mechanical factors at the nanoscale interface originated from mechanical stress, and the SEI component influenced the capacity degradation. Surface morphological changes during the initial processes may be a starting point for the physical degradation of anode materials that exhibit large volumetric changes.

References

1. Ryu J, Hong D, Lee HW, Park S (2017) Practical considerations of Si-based anodes for lithium-ion battery applications. Nano Res 10(12):3970–4002. https://doi.org/10.1007/s12274-017-1692-2

2. de las Casas C, Li WZ (2012) A review of application of carbon nanotubes for lithium ion battery anode material. J Power Sources 208:74–85. https://doi.org/10.1016/j.jpowsour.2012.02.013

3. Reimers JN, Dahn JR (1992) Electrochemical and in situ X-ray-diffraction studies of lithium intercalation in Li_xCoO_2. J Electrochem Soc 139(8):2091–2097. https://doi.org/10.1149/1.2221184

4. Ashuri M, He QR, Shaw LL (2016) Silicon as a potential anode material for Li-ion batteries: where size, geometry and structure matter. Nanoscale 8(1):74–103. https://doi.org/10.1039/c5nr05116a

5. Shi FF, Song ZC, Ross PN, Somorjai GA, Ritchie RO, Komvopoulos K (2016) Failure mechanisms of single-crystal silicon electrodes in lithium-ion batteries. Nat Commun 7:11886. https://doi.org/10.1038/ncomms11886

6. Lee SW, McDowell MT, Berla LA, Nix WD, Cui Y (2012) Fracture of crystalline silicon nanopillars during electrochemical lithium insertion. Proc Natl Acad Sci U S A 109(11):4080–4085. https://doi.org/10.1073/pnas.1201088109

7. Yang H, Huang S, Huang X, Fan FF, Liang WT, Liu XH, Chen LQ, Huang JY, Li J, Zhu T, Zhang SL (2012) Orientation-dependent interfacial mobility governs the anisotropic swelling in lithiated silicon nanowires. Nano Lett 12(4):1953–1958. https://doi.org/10.1021/nl204437t

8. Chae S, Choi SH, Kim N, Sung J, Cho J (2020) Integration of graphite and silicon anodes for the commercialization of high-energy lithium-ion batteries. Angew Chem Int Ed Engl 59(1):110–135. https://doi.org/10.1002/anie.201902085

9. Liu XH, Zhong L, Huang S, Mao SX, Zhu T, Huang JY (2012) Size-dependent fracture of silicon nanoparticles during lithiation. ACS Nano 6(2):1522–1531. https://doi.org/10.1021/nn204476h

10. McDowell MT, Lee SW, Harris JT, Korgel BA, Wang CM, Nix WD, Cui Y (2013) In situ TEM of two-phase lithiation of amorphous silicon nanospheres. Nano Lett 13(2):758–764. https://doi.org/10.1021/nl3044508

11. Su MR, Wang ZX, Guo HJ, Li XH, Huang SL, Xiao W, Gan L (2014) Enhancement of the cyclability of a Si/Graphite@Graphene composite as anode for lithium-ion batteries. Electrochim Acta 116:230–236. https://doi.org/10.1016/j.electacta.2013.10.195

12. Lee DH, Shim HW, Kim DW (2014) Facile synthesis of heterogeneous Ni-Si@C nanocomposites as high-performance anodes for Li-ion batteries. Electrochim Acta 146:60–67. https://doi.org/10.1016/j.electacta.2014.08.103

13. Okuno R, Yamamoto M, Kato A, Takahashi M (2021) Microscopic observation of nanoporous $Si-Li_3PS_4$ interface in composite anodes with stable cyclability. Electrochem Commun 130:4. https://doi.org/10.1016/j.elecom.2021.107100

14. Shobukawa H, Shin J, Alvarado J, Rustomji CS, Meng YS (2016) Electrochemical reaction and surface chemistry for performance enhancement of a Si composite anode using a bis(fluorosulfonyl) imide-based ionic liquid. J Mater Chem A 4(39):15117–15125. https://doi.org/10.1039/C6TA06447G

15. Peled E, Golodnitsky D, Ardel G, Menachem C, Tow DB, Eshkenazy V (1995) The role of SEI in lithium and lithium ion batteries, Symposium on Materials for Electrochemical Energy Storage and Conversion – Batteries, Capacitors and Fuel Cells, at the 1995 MRS Spring Meeting, Materials Research. Società, San Francisco, CA:209–221

16. McBrayer JD, Rodrigues MF, Schulze MC, Abraham DP, Apblett CA, Bloom I, Carroll GM, Colclasure AM, Fang C, Harrison KL, Liu G, Minteer SD, Neale NR, Veith GM, Johnson CS, Vaughey JT, Burrell AK, Cunningham B (2021) Calendar aging of silicon-containing batteries. Nat Energy 6(9):866–872. https://doi.org/10.1038/s41560-021-00883-w

17. Wu F, Dong Y, Su YF, Wei CX, Chen TR, Yan WA, Ma SY, Ma L, Wang B, Chen L, Huang Q, Cao DY, Lu Y, Wang M, Wang L, Tan GQ, Wang JH, Li N (2023) Benchmarking the effect of particle size on silicon anode materials for lithium-ion batteries. Small 19(42):e2301301. https://doi.org/10.1002/smll.202301301

18. Shiraki S, Shirasawa T, Suzuki T, Kawasoko H, Shimizu R, Hitosugi T (2018) Atomically well-ordered structure at solid electrolyte and electrode interface reduces the interfacial resistance. ACS Appl Mater Interfaces 10(48):41732–41737. https://doi.org/10.1021/acsami.8b08926

19. Hikima K, Shimizu K, Kiuchi H, Hinuma Y, Suzuki K, Hirayama M, Matsubara E, Kanno R (2022) Reaction mechanism of Li_2MnO_3 electrodes in an all-solid-state thin-film battery analyzed by operando hard X-ray photoelectron spectroscopy. J Am Chem Soc 144(1):236–247. https://doi.org/10.1021/jacs.1c09087

20. Chen CG, Zhou T, Danilov DL, Gao L, Benning S, Schön N, Tardif S, Simons H, Hausen F, Schülli TU, Eichel RA, Notten PHL (2020) Impact of dual-layer solid-electrolyte interphase inhomogeneities on early-stage defect formation in Si electrodes. Nat Commun 11(1):3283. https://doi.org/10.1038/s41467-020-17104-9

21. Bose S, Mandal S, Barua AK, Mukhopadhyay S (2020) Properties of boron doped ZnO films prepared by reactive sputtering method: application to amorphous silicon thin film solar cells. J Mater Sci Technol 55:136–143. https://doi.org/10.1016/j.jmst.2019.12.004

22. Sakabe J, Ohta N, Ohnishi T, Mitsuishi K, Takada K (2018) Porous amorphous silicon film anodes for high-capacity and stable all-solid-state lithium batteries. Commun Chem 1:9

23. Veith GM, Baggetto L, Sacci RL, Unocic RR, Tenhaeff WE, Browning JF (2014) Direct measurement of the chemical reactivity of silicon electrodes with $LiPF_6$-based battery electrolytes. Chem Commun (Camb) 50(23):3081–3084. https://doi.org/10.1039/c3cc49269a

24. Monteiro OR (2001) Thin film synthesis by energetic condensation. Annu Rev Mater Res 31(1):111–137. https://doi.org/10.1146/annurev.matsci.31.1.111

25. Brown IG (1998) Cathodic arc deposition of films. Annu Rev Mater Sci 28(1):243–269. https://doi.org/10.1146/annurev.matsci.28.1.243

26. Sakamoto N, Kogo Y, Yasuno T, Taniguchi J, Miyamoto I (2008) Analysis on microstructure of interface layer in DLC/Si structures produced by FIB-CVD. Diam Relat Mater 17(7–10):1706–1709. https://doi.org/10.1016/j.diamond.2008.01.058

27. Fairley N, Fernandez V, Richard-Plouet M, Guillot-Deudon C, Walton J, Smith E, Flahaut D, Greiner M, Biesinger M, Tougaard S, Morgan D, Baltrusaitis J (2021) Systematic and collaborative approach to problem solving using X-ray photoelectron spectroscopy. Applied Surface Science Advances 5:100112–100120. https://doi.org/10.1016/j.apsadv.2021.100112

28. Fang D, He F, Xie JL, Xue LH (2020) Calibration of binding energy positions with C1s for XPS results. J Wuhan Univ Technol Mater Sci Ed 35(4):711–718. https://doi.org/10.1007/s11595-020-2312-7

29. Yogi P, Tanwar M, Saxena SK, Mishra S, Pathak DK, Chaudhary A, Sagdeo PR, Kumar R (2018) Quantifying the short-range order in amorphous silicon by Raman scattering. Anal Chem 90(13):8123–8129. https://doi.org/10.1021/acs.analchem.8b01352

30. Seidlhofer BK, Jerliu B, Trapp M, Hüger E, Risse S, Cubitt R, Schmidt H, Steitz R, Ballauff M (2016) Lithiation of crystalline silicon as analyzed by operando neutron reflectivity. ACS Nano 10(8):7458–7466. https://doi.org/10.1021/acsnano.6b02032

31. Parratt LG (1954) Surface studies of solids by total reflection of X-rays. Phys Rev 95(2):359–369. https://doi.org/10.1103/PhysRev.95.359

32. Stömmer R, Martin AR, Hub W, Göbel H, Pietsch U (1999) X-ray scattering from silicon surfaces: a useful tool for quality control. Microelectron Eng 45(2–3):257–263. https://doi.org/10.1016/S0167-9317(99)00170-7

33. Ma HP, Yang JH, Yang JG, Zhu LY, Huang W, Yuan GJ, Feng JJ, Jen TC, Lu HL (2019) Systematic study of the SiOx film with different stoichiometry by plasma-enhanced atomic layer deposition and its application in SiOx/SiO2 super-lattice. Nanomaterials 9(1):13. https://doi.org/10.3390/nano9010055

34. Obrovac MN, Krause LJ (2007) Reversible cycling of crystalline silicon powder. J Electrochem Soc 154(2):A103–A108. https://doi.org/10.1149/1.2402112

35. Chan CK, Ruffo R, Hong SS, Huggins RA, Cui Y (2009) Structural and electrochemical study of the reaction of lithium with silicon nanowires. J Power Sources 189(1):34–39. https://doi.org/10.1016/j.jpowsour.2008.12.047

36. Uxa D, Jerliu B, Hüger E, Dörrer L, Horisberger M, Stahn J, Schmidt H (2019) On the lithiation mechanism of amorphous silicon electrodes in Li-ion batteries. J Phys Chem C 123(36):22027–22039. https://doi.org/10.1021/acs.jpcc.9b06011

37. Philippe B, Dedryvère R, Allouche J, Lindgren F, Gorgoi M, Rensmo H, Gonbeau D, Edström K (2012) Nanosilicon electrodes for lithium-ion batteries: interfacial mechanisms studied by hard and soft X-ray photoelectron spectroscopy. Chem Mater 24(6):1107–1115. https://doi.org/10.1021/cm2034195

38. Pereira-Nabais C, Świątowska J, Chagnes A, Ozanam F, Gohier A, Tran-Van P, Cojocaru CS, Cassir M, Marcus P (2013) Interphase chemistry of Si electrodes used as anodes in Li-ion batteries. Appl Surf Sci 266:5–16. https://doi.org/10.1016/j.apsusc.2012.10.165

39. Cangaz S, Hippauf F, Reuter FS, Doerfler S, Abendroth T, Althues H, Kaskel S (2020) Enabling high-energy solid-state batteries with stable anode interphase by the use of columnar silicon anodes. Adv Energy Mater 10(34). https://doi.org/10.1002/aenm.202001320

40. Takezawa H, Ito S, Yoshizawa H, Abe T (2017) Surface composition of a SiOx film anode cycled in carbonate electrolyte for Li-ion batteries. Electrochim Acta 229:438–444. https://doi.org/10.1016/j.electacta.2017.01.138

41. Veith GM, Doucet M, Sacci RL, Vacaliuc B, Baldwin JK, Browning JF (2017) Determination of the solid electrolyte interphase structure grown on a silicon electrode using a fluoroethylene carbonate additive. Sci Rep 7(1):6326. https://doi.org/10.1038/s41598-017-06555-8

42. Yin YL, Arca E, Wang LN, Yang G, Schnabel M, Cao L, Xiao CX, Zhou HY, Liu P, Nanda J, Teeter G, Eichhorn B, Xu K, Burrell A, Ban CM (2020) Nonpassivated silicon anode surface. ACS Appl Mater Interfaces 12(23):26593–26600. https://doi.org/10.1021/acsami.0c03799

43. Cao CT, Abate II, Sivonxay E, Shyam B, Jia CJ, Moritz B, Devereaux TP, Persson KA, Steinrück HG, Toney MF (2019) Solid electrolyte interphase on native oxide-terminated silicon anodes for Li-ion batteries. Joule 3(3):762–781. https://doi.org/10.1016/j.joule.2018.12.013

44. Tasaki K, Goldberg A, Lian JJ, Walker M, Timmons A, Harris SJ (2009) Solubility of lithium salts formed on the lithium-ion battery negative electrode surface in organic solvents. J Electrochem Soc 156(12):A1019–A1027. https://doi.org/10.1149/1.3239850

45. Han B, Zhang Z, Zou YC, Xu K, Xu GY, Wang H, Meng H, Deng YH, Li J, Gu M (2021) Poor stability of Li_2CO_3 in the solid electrolyte interphase of a lithium-metal anode revealed by cryo-electron microscopy. Adv Mater 33(22):10. https://doi.org/10.1002/adma.202100404

46. Kim J, Chae OB, Lucht BL (2021) Perspective—structure and stability of the solid electrolyte interphase on silicon anodes of lithium-ion batteries. J Electrochem Soc 168(3):6. https://doi.org/10.1149/1945-7111/abe984

47. Wang HR, Chew HB (2017) Nanoscale mechanics of the solid electrolyte interphase on lithiated-silicon electrodes. ACS Appl Mater Interfaces 9(31):25662–25667. https://doi.org/10.1021/acsami.7b07626

48. Kim SH, Dong K, Zhao H, El-Zoka AA, Zhou XY, Woods EV, Giuliani F, Manke I, Raabe D, Gault B (2022) Understanding the degradation of a model Si anode in a Li-ion battery at the atomic scale. J Phys Chem Lett 13(36):8416–8421. https://doi.org/10.1021/acs.jpclett.2c02236